# Applications of Synchrotron Radiation to Defect Characterization and *Pendellösung* Fringe-Spacing Measurement in a Natural Diamond

## A. R. Lang,[a] G. Pang[a] and A. P. W. Makepeace[b]

[a]*H. H. Wills Physics Laboratory, University of Bristol, Tyndall Avenue, Bristol BS8 1TL, UK, and* [b]*Department of Physiology, School of Medicine, University of Bristol, Bristol BS8 1TD, UK*

A small polished rectangular block of natural diamond unusually free from impurity zoning was examined by birefringence and synchrotron X-ray topography to map internal defects and assess effects of some accidental mechanical damage. 'Orthogonal-view' projection topographs facilitated comparisons between optical and X-ray images. Speedy and precise positioning of crystal sections cut in synchrotron X-ray section topographic studies was aided by radiographic and fluoroscopic procedures, which are described. Several X-ray reflection and refraction phenomena are illustrated, including high-contrast refraction images of crystal edges, chipping and crack outcrops. It was demonstrated that by combining optical and X-ray goniometry it was possible to record *Pendellösung* fringe systems employing precisely selected X-ray wavelengths in well defined crystal volumes. Valuable gain in fringe visibility resulted from the use of pure $\sigma$-mode polarized synchrotron radiation. Absolute values of the diamond 004 structure factor were derived from five fringe systems measured, the findings (in upward order) being 11.7, 11.7, 12.0, 12.5, 12.6. Their scatter greatly exceeds the uncertainty in the measurement procedure (believed to be within ±1%) and is attributed to different strain distributions within the five volumes sampled.

**Keywords: diamond; X-ray topography;** *Pendellösung*; **X-ray refraction contrast; structure-factor measurement; defects.**

## 1. Introduction

The notorious inhomogeneity of impurity and lattice defect content in diamonds, both natural and synthetic, requires that characterization experiments performed on these specimens (by X-ray diffraction or optical methods, for instance) should be capable of probing the specimen's properties point-by-point. This entails using one or more of the topographic defect-imaging methods applicable to diamonds (Lang, 1993, 1994). Given a specimen possessing a pair of opposite facets, either mechanically polished or (a rare occurrence) naturally occurring smooth and flat, then the birefringence pattern viewed through the facets provides a simple yet highly sensitive indicator of the dislocation population and other strain-producing defects within the specimen's interior. X-ray topography is applicable equally for probing diamond interiors or for studying strain-producing surface and near-surface defects. It is good at establishing the nature of the sources of diffraction contrast. For such diagnosis it is very helpful to have a wide range of X-ray wavelengths available. This requirement is well met by applying white-radiation synchrotron X-ray topography to diamond assessment.

The specimen whose examination by synchrotron X-ray topography is described here was one chosen for lattice-parameter measurement by the divergent-beam pseudo-Kossel method (Lonsdale, 1947; Lang & Pang, 1996). A modern development of this method, giving higher angular resolution than that available to Lonsdale (1947), combined with application to specimens selected for their high lattice perfection, provided the conditions needed for novel observations of certain fine structures in the Kossel pattern. These structures arise from coherent multiple diffraction effects (Lang, 1995; Lang & Pang, 1995). Their manifestation in Kossel patterns produced by the present specimen was evidence of good lattice perfection, confirming inference of such quality from the exceptionally low birefringence that had been one of its qualifications for use in lattice-parameter measurements. Unfortunately, during one mounting of the crystal for such experiments it was accidentally mechanically damaged (details given in §2) and some strain birefringence was created. This prompted comparative studies of its birefringence and X-ray topographic images. The freedom in Bragg-angle selection afforded by continuous-spectrum X-rays was exploited by taking 'orthogonal-view' projection topographs, facilitating comparison with optical micrographs, and illustrated in §3. During work reported in §3 and later, various X-ray refraction and reflection effects were observed; they are discussed in §4.

A second aim of the work was a structure-factor determination from *Pendellösung* fringe-spacing measurements on synchrotron-radiation section topographs. Efficient procedures for taking section topographs with a synchrotron radiation source are outlined in §5. The *Pendellösung* measurements are presented in §6, where it is explained how the wavelength of *Pendellösung* patterns recorded was established by combining optical and X-ray goniometry.

## 2. The specimen

The specimen was a polished rectangular block, dimensions $1 \times 1 \times 2 \, mm^3$, that had been cut from a natural diamond (source unknown, but probably S. Africa). The long dimension of the block was parallel to a crystallographic cube axis, and the major $2 \times 1$ mm faces were polished parallel to {110}. The scientific importance of this specimen lay in its exceptional homogeneity of content of nitrogen (the dominant known impurity in both natural and synthetic diamonds) coupled with the fact that the nitrogen was present almost entirely in the form of 'A-defects'. [The accepted structure of these point defects is a pair of N atoms substitutionally occupying adjacent atomic sites in the diamond structure (Davies, 1976; Clark, Collins & Woods, 1992).] However, it was the singular freedom

from birefringence (referred to in §1) that most patently testified to homogeneity of impurity content and consequent uniformity of lattice parameter.

For Kossel-pattern recording the crystal was placed in the specimen chamber of a scanning electron microscope. A focused electron beam, diameter $\leq 10 \, \mu m$, impinged on a 2 μm-thick evaporated Cu layer on one of the large faces of the specimen; the divergent-beam diffraction pattern to be recorded emerged from an opposite face. In some early experiments the required temperature control of the specimen was achieved by clamping it in contact with a heat sink, the clamping being effected by a brass bar covering one of the specimen's major faces. The bar lay parallel to the long dimension of the specimen and extended beyond its ends so as to accommodate a holding-down bolt some distance from each end of the specimen. Overtightening of these bolts caused elastic arching of the bar, bringing concentrated stress to bear on the edges of the specimen where the clamped face and the end facets met. Chipping and cracking that ensued was localized, fortunately, but visible birefringence associated with the cracks extended into a significant fraction of the whole specimen volume. Fig. 1 is a reflected-light micrograph of one of the major faces of the specimen, that face indexed ($\bar{1}\bar{1}0$). Both corners at the top of the image have lost chips, and below the top right-hand corner the diffuse darkening seen is due to an interior crack that prevents reflection of light from the far surface, *i.e.* from surface (110). Darkening of similar origin is seen at the bottom right-hand corner of the print. These represent some of the features producing birefringence and diffraction contrast described in §3.

In order to make quantitative use of the *Pendellösung* fringe-spacing measurements described in §6, various interfacial angles of the specimen need to be known accurately. Frequent reference will be made to the
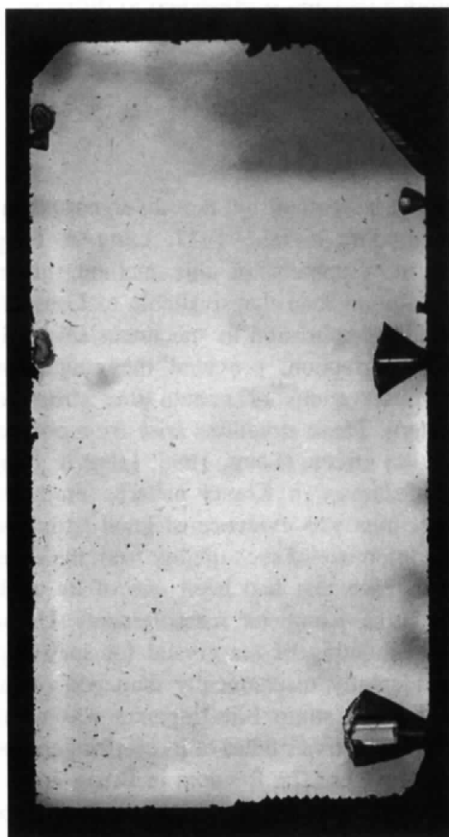


**Figure 1**
Reflected-light optical micrograph of the specimen prism face indexed ($\bar{1}\bar{1}0$), called face (*c*); [001] points to the top of the image. Some light is reflected from the face below, which is out of focus; chips on it or cracks near it appear as diffuse darkenings.
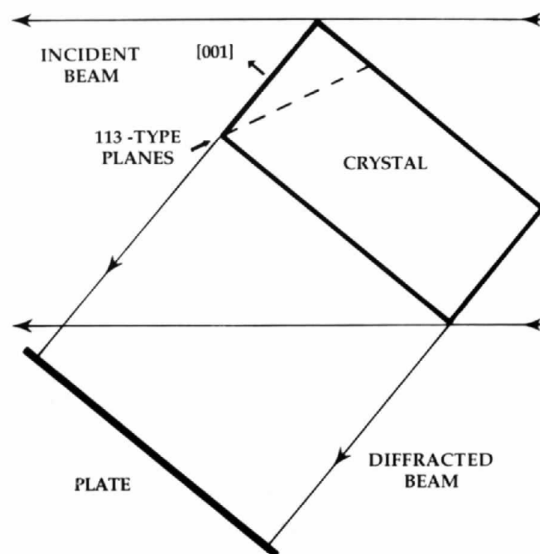


**Figure 2**
Diffraction geometry for 'orthogonal-view' synchrotron-radiation projection topographs; the 113-type diffracted beam leaves the crystal perpendicular to one pair of its polished prism faces. Crystal-to-plate distance ~50 mm in practice.

specimen's four near-{110}-orientation prism faces. For convenience these are given a short-hand notation as follows. Looking at the square end facet indexed (001), the surrounding prism faces seen edge-on, listed in a clockwise cycle, are named (a) for (110), (b) for (1$\bar{1}$0), (c) for ($\bar{1}\bar{1}$0) and (d) for ($\bar{1}$10). Smoothness and flatness of the polished surfaces was good enough to give optical goniometric signals measurable to one minute of arc or better. The *internal* angles between adjacent prism faces measured by optical goniometry were: (b)$^\wedge$(a) 89°12', (c)$^\wedge$(b) 90°44', (d)$^\wedge$(c) 89°18', (a)$^\wedge$(d) 90°46'. Note close parallelism of (a) with (c) and of (b) with (d). No specimen taper needing measurement was apparent. Distances between (a) and (c) and between (b) and (d) are 1.035 and 1.045 mm, respectively, measured by micrometer. Knowledge of the angle between the geometric axis of the specimen prism and the normal to the end facet called (001) was needed. Optical goniometry found this angle to be small: the end-facet normal had tilt components 9.5' towards face (c) and 8.5' towards face (d).

## 3. Correlation of birefringence and X-ray topographic observations

X-ray topography was performed at the SRS, Daresbury Laboratory, on Station 7.6, 80 m from the tangent point,

using the double-crystal camera (Bowen & Davies, 1983) in single-crystal mode. Fig. 2 shows the diffraction geometry employed to obtain orthogonal views of the crystal by setting the Bragg angle equal to that between (001) and planes of form {113}, 25.24°. The corresponding wavelength is 0.092 nm, very suitable for X-ray topography of diamond specimens ~1 mm thick (Lang, Makepeace, Moore & Machado, 1983). Crystal setting was facilitated by optical reflections from its surfaces, using a pinhole-collimated laser beam parallel to, but oppositely directed to, the incident X-rays. In all X-ray experiments real-time TV viewing of a fluorescent screen downstream of the specimen speeded adjustment of slits defining incident-beam size and shape. The four 'orthogonal-view' projection topographs taken with reflections 113, $\bar{1}$13, $\bar{1}\bar{1}$3 and 1$\bar{1}$3 provided a good record of both grown-in defects and mechanical damage. They were compared with reflected-light micrographs (exemplified by Fig. 1) and with the corresponding transmitted-light birefringence micrographs. A few examples are shown here, illustrating information gained through X-ray and optical examinations, either separately or in combination.

Figs. 3(a) and 3(b) are birefringence micrographs taken with light transmitted through the crystal from face (a) to face (c). [These views showed much stronger birefringence than those taken with light transmitted between faces (b) and (d).] Principal interest in Fig. 3 lies in comparison
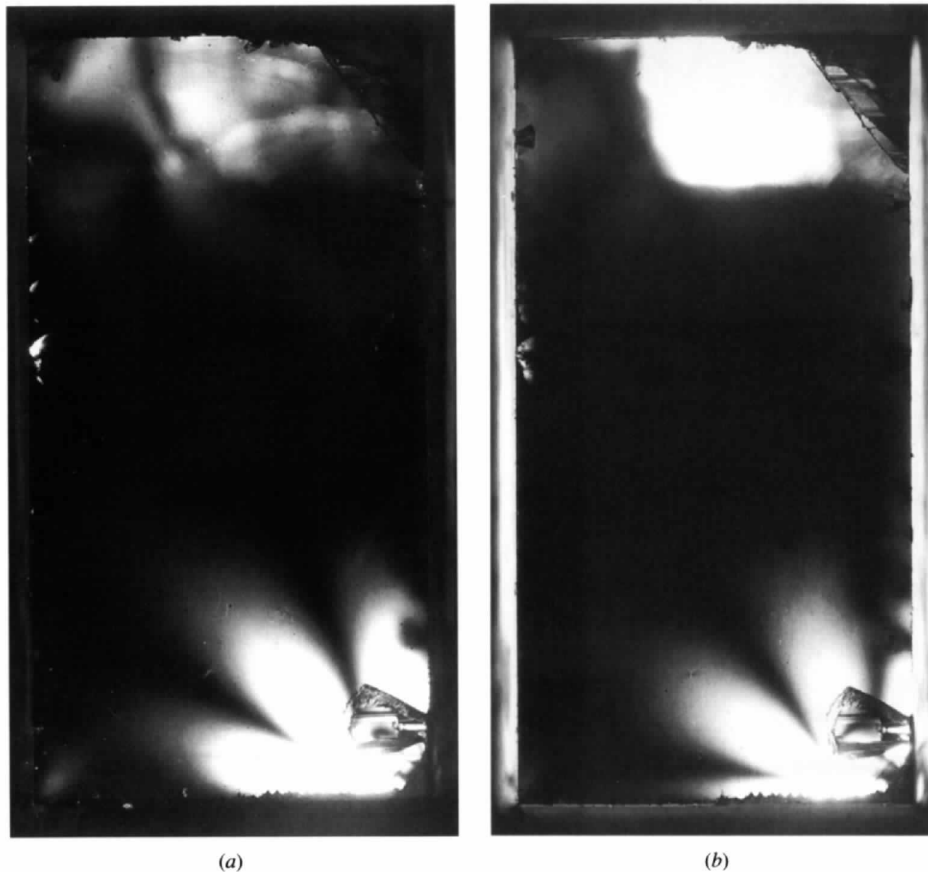


(a)    (b)

**Figure 3**
Birefringence patterns produced by the specimen oriented as in Fig. 1. Axes of crossed polarizers are parallel to specimen edges in (a) and at 45° to them in (b).

with X-ray topographs, but a few points arising through comparison with Fig. 1 are worth mentioning. Birefringence due to the large crack at the (001) end of the specimen does not extend far beyond the crack surface recognizable visually. On the other hand, the much smaller crack seen in the bottom right corner, in this view, radiates large lobes of strain birefringence. Note how lobes of extinction and transmission interchange between Figs. 3(a) and 3(b).

In order to establish the distribution of diffraction-contrast-producing defects within the volume of the crystal, close comparison of the four X-ray projection topographs was needed, in particular to find the distances of observed defects from the X-ray exit face in each case, no stereo-topographs having been taken. The general resemblance between images recorded with (a) and (c) serving as X-ray exit surfaces, and likewise with (b) and (d) so used, justifies displaying only one from each pair in order to show essential features of the images. Fig. 4(a) was taken with face (c) as X-ray exit surface, and Fig. 5(a) with face (b) acting thus. Before comparing X-ray and birefringence images of some features individually, a generic identification of important sources of diffraction contrast observed is provided by lettering on the accompanying diagrams Figs. 4(b) and 5(b), indicating

as follows: C, cracks (or patches of diffraction contrast arising therefrom); E, chipping along or close to edges; S, scratches, chiefly polishing striae running vertically on the images, oriented parallel to the conventional cube-axis polishing direction; P, percussion damage; and D, grown-in dislocations.

Local deformation associated with the crack that generates the strong birefringence seen at the bottom right corner of Figs. 3(a) and 3(b) is sufficient to produce 'flaring' on the topograph image of that corner, indicating misorientations of several minutes of arc. A crack cutting across the top right corner of face (b) separates off a wedge of intensely diffracting distorted material, detectably misoriented from the bulk of the specimen though by less than a minute of arc. The strongly visible group of at least three dislocations running across Fig. 5(a), near the image top, outcrop on face (b) close to the second crack described above. The single dislocation running ca 0.25 mm below this group on Fig. 5(a) and following a roughly similar trajectory is seen to outcrop on face (b) near its vertical median line. Crossing this dislocation image is that of another dislocation, more remote from face (b), taking a different trajectory [and seen in the $\bar{1}\bar{1}3$ topograph to outcrop on face (a) very close to the (a)/(d) edge]. All these dislocations are visible in
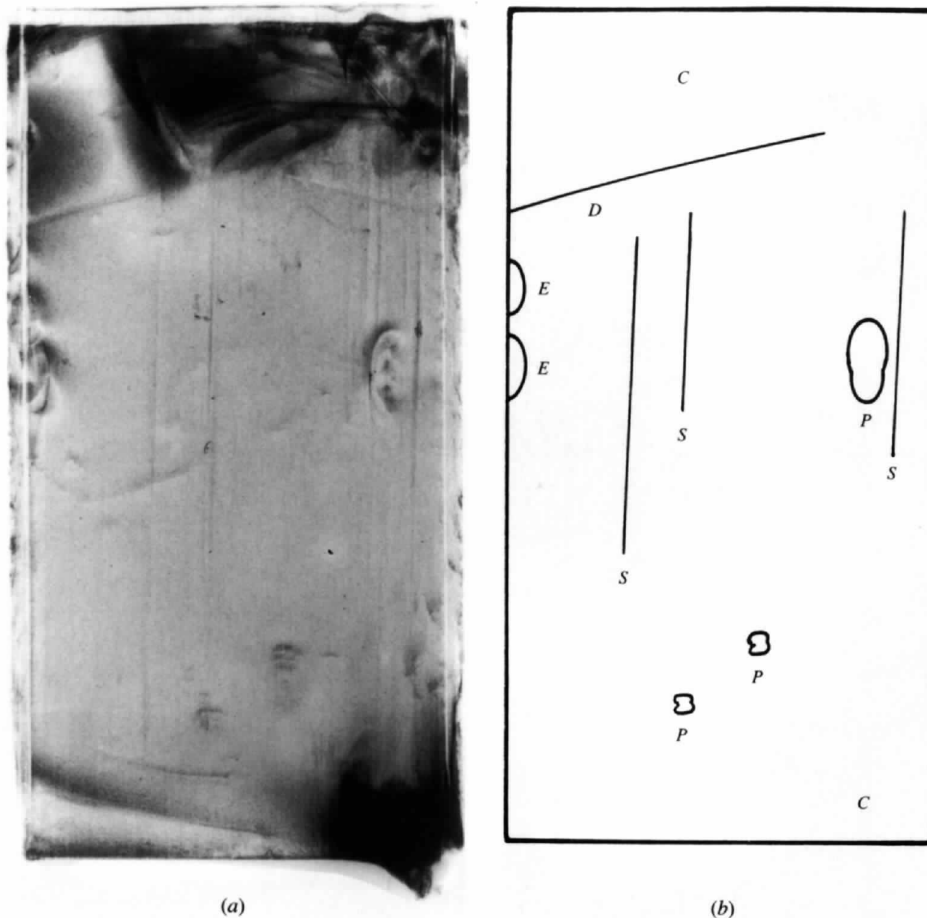


(a)

(b)

**Figure 4**
(a) Projection topograph, face (c) facing observer, reflection 113, wavelength 0.092 nm. Same view of crystal as in Figs. 1 and 3. (All X-ray topographs were recorded on Ilford L4 nuclear plates, emulsion thickness 25 μm, and all are reproduced as viewed looking towards the crystal.) (b) Identification of some diffraction-contrast features on (a). Lettering explained in text.

all four 113-type reflections, albeit weakly in some cases. Their Burgers vectors were not determined. Close examination of birefringence viewed through face (b) showed just-detectable birefringence images of the first-mentioned dislocation group, despite proximity of birefringence due to mechanical damage. (In the absence of this damage, birefringence images of individual dislocations would have been easily detectable in a diamond matrix so free from birefringence due to impurity zoning, according to previous experience). Regarding implications for the Kossel-pattern experiments it can be concluded that since it was the central volume of the specimen that was traversed by X-rays in that work, neither the few dislocations near the (001) end of the specimen nor the mechanical damage concentrated at the specimen ends gave cause for concern.

## 4. Refraction and reflection phenomena

The excellent incident beam collimation resulting from the 80 m source-to-specimen distance, coupled with use of specimen-to-plate distances generally not less than a few cm, bring to light various X-ray reflection and refraction effects, which become especially noticeable in the case of faceted specimens. For example, in Fig. 4(a) one sees white lines running vertically on the image, close to its left and right margins. They arise from refraction. Fig. 6

shows how. The left-hand white line was identified as the image of prism edge S between faces (d) and (c), and that on the right as the image of edge Q between faces (a) and (b). It happened that when this topograph was taken the specimen had suffered an accidental rotational mis-setting about the prism axis, by ca 2° anticlockwise looking down on the (001) facet. In Fig. 6, incident ray 1, exiting as diffracted ray 1', exemplifies rays undeviated by refraction (for all practical purposes). Incident ray 2 enters PQ close to P, makes a grazing emergence from PS close to P, being deviated to the left, and forms the left-hand boundary of the topograph image (ray $\tilde{2}$). Correspondingly, ray 5 makes a grazing entry into face QR close to R, is thereby deviated rightward, and emerges from SR (without further refractive deviation) to form the topograph's right-hand boundary (ray $\tilde{5}$). Grant to incident rays 3 and 4 a finite spatial width, sufficient to straddle prism edges S and Q, respectively. They then emerge split into refraction-deviated components ($\tilde{3}$ and $\tilde{4}$) and undeviated components (3' and 4'). No diffracted rays emerge in directions between $\tilde{3}$ and 3', nor between 4' and $\tilde{4}$. Hence the white lines. {In Fig. 6 necessary strong exaggeration of refractive deviations causes the spatial width between $\tilde{2}$ and $\tilde{3}$ to appear greater than that between $\tilde{4}$ and $\tilde{5}$. In fact, as Fig. 4(a) shows, these spatial widths on the topograph are almost the same, because PS [face (d)] is so nearly parallel to QR [face
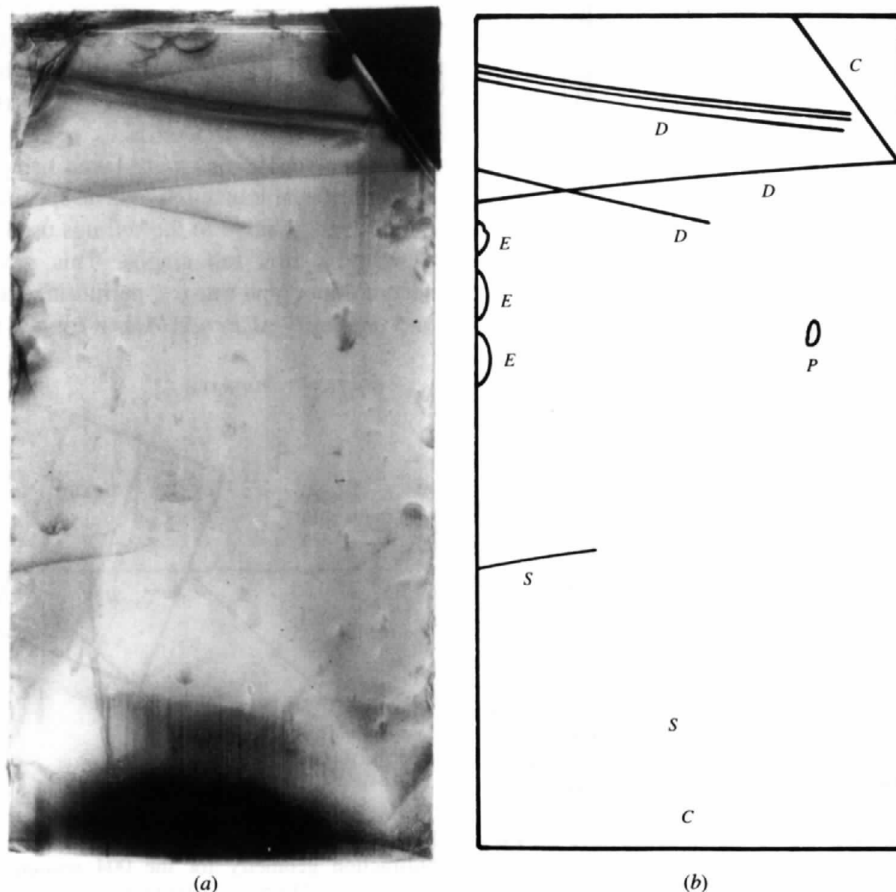


(a)                                    (b)

**Figure 5**
(a) Projection topograph, face (b) facing observer, reflection $\bar{1}13$, wavelength 0.092 nm. (b) Identification of some features on (a).

(*b*), as mentioned in §2.} Fig. 4(*a*) exhibits another feature arising from refraction. A fine line of diffracted X-rays lies parallel to and above the top edge of the image. These rays have been refracted out of the (001) facet; their angular displacement upwards from rays emerging from face (*c*) is about a quarter of the critical angle, which is 10′ for the wavelength used.

Somewhat different circumstances are the cause of other 'mirage-like' extra images that appear on the 1̄13 topograph, reproduced in Fig. 5(*a*). In this case there can be seen (certainly on the original plates and micrographs) fine lines of weak diffracted intensity running parallel to the long edges of the main image and separated outwards from it by 40 μm on the left and by (on average) 70 μm on the right. These extra rays arise because the sum of the included angle between the near face (*b*) and the adjacent face (*c*) on the left (90°44′) plus that between (*b*) and (*a*) adjacent on the right (89°12′) falls 4′ short of 180°. Thus with face (*b*) set very close to normal to the plane
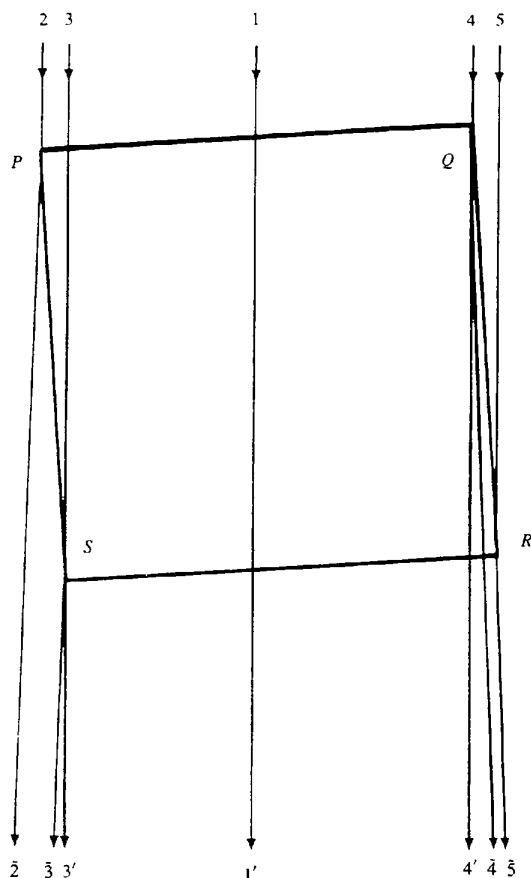


**Figure 6**
Origin of the refraction-produced white lines apparent close to the left and right margins of topograph Fig. 4(*a*). Ray paths viewed projected on (001). The anticlockwise rotational mis-setting of specimen *PQRS* about [001] is exaggerated twofold; ray deviations due to refraction are exaggerated 200-fold. In the setting of Fig. 4(*a*) the correspondence with the specimen prism face is: *PQ*, (*a*); *QR*, (*b*); *RS*, (*c*); *SP*, (*d*). The incident rays numbered 1–5 at the diagram top are parallel to each other. The directions taken by diffracted rays, numbered at the bottom of the diagram, are explained in the text.

of incidence, both adjacent faces (*a*) and (*c*) satisfy the Bragg surface-reflecting condition. However, at faces (*a*) and (*c*) the surface-grazing incidence and reflection angles are both very small since the diffraction vector and surface normal are almost orthogonal in each case. The resulting specular component added to the directions of diffracted rays causes the outward displacements observed, which have magnitudes consistent with the goniometric data.

In none of the X-ray refraction manifestations seen in this work were the special diffraction geometrical conditions present that permit double refraction under Bragg-diffraction conditions to be observed (Lang, Kowalski, Makepeace & Moore, 1986). However, simple single refraction served very usefully to delineate crystal edges, as described in the following section.

## 5. Section topography

When taking section topographs with a synchrotron-radiation source it is often more convenient to change the location of specimen sections by translating the ribbon incident X-ray beam rather than by translating the specimen relative to a spatially-fixed incident beam as is done on conventional topograph cameras operated with conventional sources. In the present work the slit defining the incident beam was mounted on a micrometre-screw-operated slide attached to a tower fitted with a standard optical-bench carriage at its base. The carriage sat on an optical bench parallel to the synchrotron-beam axis (an integral part of the camera construction). Thus the whole incident-beam-slit assembly could be quickly taken off the camera, and reproducibly replaced on it.

Section topographs were taken using the 004 reflection in symmetrical transmission. The specimen was rotated 45° about [001] relative to the settings used for the orthogonal-view projection topographs. This gave rhombus-shaped section topograph images, permitting study of the visibility and regularity of *Pendellösung* fringes in the image of the
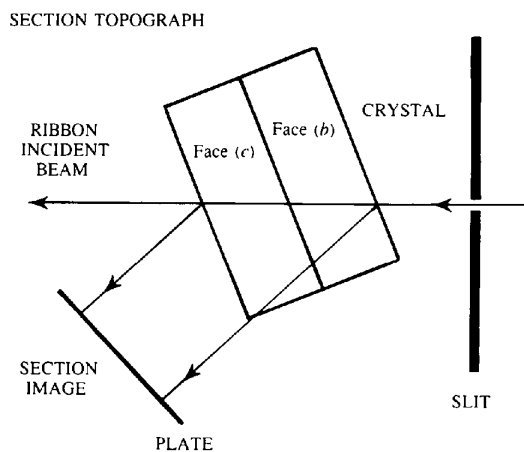


SECTION TOPOGRAPH

**Figure 7**
Diffraction geometry for the 004 section topograph shown in Fig. 8; $\theta_B$ = 21.65°, $\lambda$ = 0.066 nm. Crystal turned about its prism axis so that faces (*a*) and (*b*) are X-ray entrance surfaces, equally inclined to the X-ray beam.

wedge-shaped volumes cut by the X-rays. Use of pure $\sigma$-mode polarized synchrotron X-rays helped immensely. Fig. 7 shows the diffraction geometry and Fig. 8 is a section topograph taken with diffraction angle and incident-beam location as drawn in Fig. 7. To achieve precisely the desired location of sections cut by the incident beam, direct-beam radiographs were taken using a double-exposure technique. An exposure with the beam-defining slit in position was made on the same film as one made with the slit-carrying tower removed from the optical bench, the latter radiograph then showing the whole crystal. This procedure produced radiograph images like that drawn in Fig. 9, which illustrates the diffraction geometry applying in Figs. 7 and 8. For some applications slit-positioning could be achieved with adequate precision by TV-aided real-time fluoroscopy, comparing images on the TV screen obtained with and without the slit assembly in position.
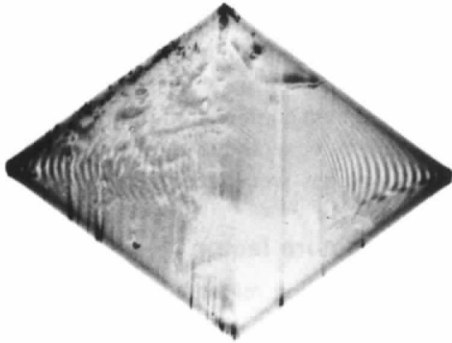
When high-resolution nuclear emulsions are used to record crystal radiographs, a wealth of detail arising from X-ray refraction effects is seen. Contrast in such structure is enhanced by using relatively large specimen-to-plate distances as in Fig. 10, though at the expense of resolution. The geometry in Fig. 10 is similar to that in Fig. 9 (minus the superimposed section-cutting beam), differing in that the Bragg angle has been increased to $\sim$46° and a small rotation of the specimen about [001] has been made to bring the edge between faces (a) and (b) into the same line of sight as the edge between (c) and (d). In the radiograph the crystal outline is accompanied by a dark band due to X-rays refracted outward, beyond the geometrical silhouette, adding intensity to the background of X-rays that do not pass through the crystal at all. Faces that meet in edges within the silhouette act as diverging biprisms; these edges show up as white lines on the radiograph. Likewise visible is the outcrop on the (001) facet, parallel to its top-left edge, of the large crack whose shadow was seen near the top edge of the optical micrograph in Fig. 1. The chip seen in Fig. 1 at the top right corner of face (c), together with the fan-shaped scalloped chip seen about halfway down the right-hand edge of face



**Figure 8**
Section topograph taken with the diffraction geometry drawn in Fig. 7. Reference to Fig. 7 explains the correspondence of image edges with crystal faces: upper left, X-ray exit face (d); upper right, X-ray exit face (c); lower left, X-ray entrance face (a); lower right, X-ray entrance face (b). Vertical streaks on the image (i.e. streaks in the plane of X-ray incidence) showing both light and dark components arise from surface damage (Lang, 1994).
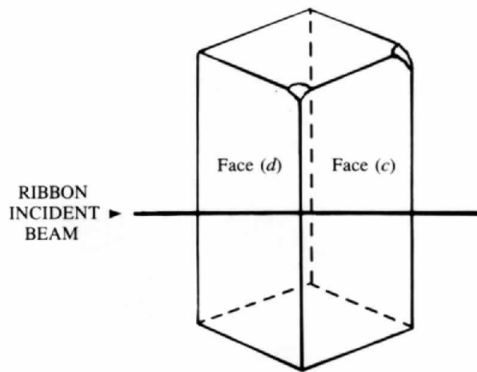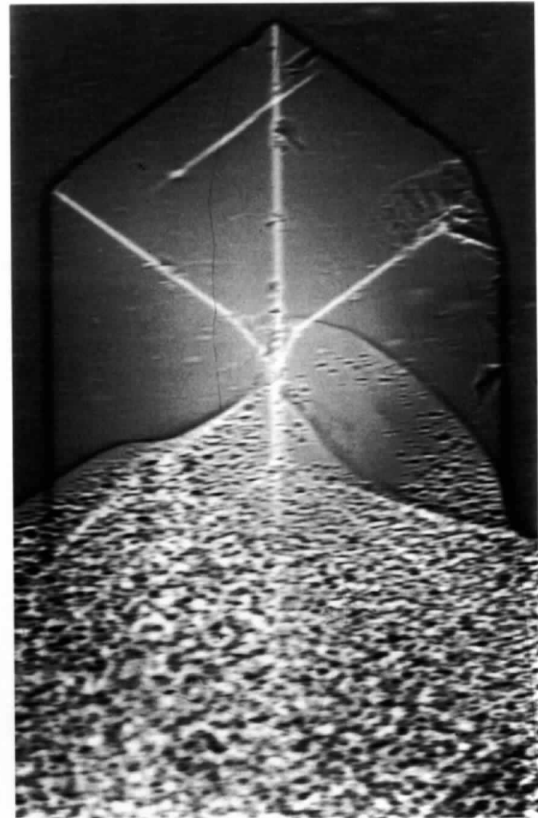


**Figure 9**
View looking towards the X-ray source, illustrating superimposition of a section-cutting X-ray beam upon a radiograph of the whole crystal, as set in Fig. 8. The two X-ray exit faces are lettered. So as to correspond with the image geometry of Fig. 8, the furthest prism edge [between faces (a) and (b)] is drawn slightly out of line with the nearest prism edge [between faces (c) and (d)].



**Figure 10**
Radiograph of the crystal set as in Figs. 8 and 9, except for a Bragg angle increase to $\sim$46° and lining-up of the nearest and furthest prism edges in the plane of incidence. Specimen-to-plate distance $\sim$60 cm. Horizontal elongation of images of small contrast-producing objects is well accounted for by the horizontal extension of the X-ray source, which is $\sim$3 mm parallel to the electron orbit plane.

(c), are also well recognizable on the right of the radiograph image in Fig. 10. The mount of Araldite into which the lower end of the specimen is set produces a strongly mottled image due to its vesicular texture; this image covers the lower part of the radiograph.

Fig. 11 is the projection topograph corresponding to the radiograph, Fig. 10. In interpreting Fig. 11, bear in mind



**Figure 11**
Projection topograph, 004 reflection, $\theta_B = 45.95°$, $\lambda = 0.128$ nm. Dominant diffraction contrast comes from cracks, and from polishing striae and other superficial damage. The specimen-to-plate distance being $<0.1$ that used for the radiograph, Fig. 10, the gross refraction mottle due to Araldite vesicles is here reduced to fine-scale speckle.

that whereas the specimen corner seen uppermost in Fig. 10 is the meeting point of the top facet with prism faces (a) and (b), that seen uppermost in Fig. 11 is the top facet's meeting with faces (c) and (d) (compare Figs. 7 and 9). The large crack whose outcrop on the top facet in the Fig. 10 view was pointed out now lies between the top left corner and the centre of the image in Fig. 11, and is responsible for the strong diffraction contrast coming from that area. Parallel to the vertical edges of the Fig. 11 image fine *Pendellösung* fringes are visible. Figs. 10 and 11 were examined together to decide at what level to cut the specimen by section topographs, so as to best avoid surface damage appearing along or close to the vertical edges of the images. Sections were taken that cut these edges about 100 µm above specimen mid-height, as viewed in Fig. 11. Figs. 12(a) and 12(b) are enlargements of the *Pendellösung*-fringe-containing areas in one of the section topographs resulting. (The section topograph Fig. 8 showed strong patchy darkening on its left half, attributed to distributed surface sources of diffraction contrast. These were traced to partial coverage by a contamination film probably acquired during cathodoluminescence studies. This highly tenacious film was removed by a combination of mechanical scraping plus soaking in hot concentrated $H_2SO_4$ before Fig. 11 and subsequent topographs were recorded.)

## 6. The 004 structure factor

The *Pendellösung* period measured on section topographs, $\Lambda_m$, is the spacing of intensity maxima (or minima) along the loci of vertices of the hook-shaped fringes that appear in Figs. 8 and 12. From $\Lambda_m$ is derived the fundamental quantity, $\Lambda_\rho$, the *Pendellösung* period in the crystal, taken along the net plane from the X-ray entrance point, in the plane of incidence. The two periods are connected by the geometrical factor $\Phi$, $\Lambda_m = \Lambda_\rho \Phi$. The relation between $\Lambda_\rho$ and the structure factor $F_g$ in the $\sigma$ polarization case applying in these synchrotron-radiation experiments is



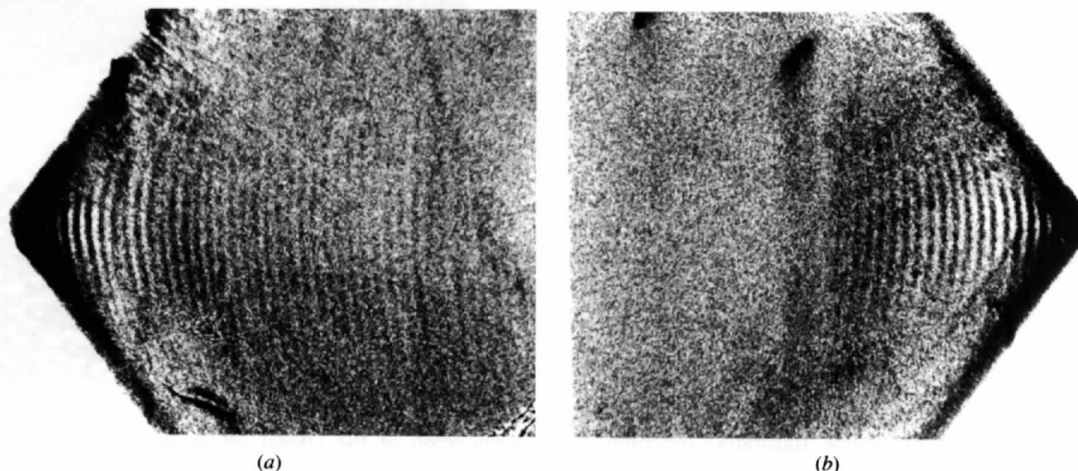(a)                                                    (b)

**Figure 12**
*Pendellösung*-containing left- and right-hand parts of a section topograph cutting the specimen near mid-height as seen in Figs. 10 and 11. Crystal setting related to that in Figs. 10 and 11 by 180° rotation about [001]. Wavelength 0.124 nm. Image 0.5 mm wide in both (a) and (b). (a) Wedge formed between specimen face (b) above left (X-ray exit) and face (c) below left (X-ray entrance). (b) Wedge formed between specimen face (a) above right (X-ray exit) and face (d) below right (X-ray entrance).

(Kato, 1969)

$$.1_p = (mc^2/e^2)(\pi V/\lambda)F_g^{-1}\cos\theta_B. \qquad (1)$$

where $V$ is the volume of the diamond unit cell ($45.38 \times 10^{-30}\,\mathrm{m}^3$) and $e^2/mc^2$ is the classical electron radius. In white-radiation experiments the value of $\lambda$ is determined by the interplanar spacing $d$ and the Bragg angle $\theta_B$ at which the crystal is set. Then the form of (1) useful for analyzing synchrotron radiation section topographs is

$$F_g = (mc^2/e^2)(\pi V/2d)(\Phi/\Lambda_m)\cot\theta_B. \qquad (2)$$

When the specimen is oriented about [001] so that a diagonal plane of the prism lies parallel to the plane of incidence (as in Figs. 10 and 11), and assuming the prism section is perfectly square and the (001) plane exactly normal to the prism axis, the factor $\Phi$ is simply 0.5. More generally, expressing $\Phi$ in terms of the internal angle $\tau$ between the prism faces forming the wedge where *Pendellösung* fringes are observed, and in terms of the angle $\alpha$, the component in the plane of incidence of the tilt of [001] off the prism axis (measured as described below), gives

$$\Phi = 0.5\cot(\tau/2)\cos\alpha. \qquad (3)$$

At the SRS, Bragg-angle settings were made starting from an initial setting with the specimen end facet [nominally of (001) orientation] precisely retroreflecting the laser beam directed antiparallel to the synchrotron beam. From optical goniometry (§2) the angle between the geometric axis of the specimen prism and $\mathbf{n}$, the normal to the end facet, was known. Viewing the plane of incidence as in Fig. 7, the angle $\beta$, the component in the plane of incidence of the tilt of $\mathbf{n}$ off the prism axis, is taken positive when $\mathbf{n}$ is rotated anticlockwise relative to the prism axis; and $\beta = 0.2°$ in this view. The component $\alpha$ is also taken positive when, similarly viewed, it is an anticlockwise rotation of [001] relative to the prism axis. It follows that when the Bragg angle is adjusted by rotating the crystal-carrying axis of the X-ray camera clockwise (as viewed in Fig. 7) by the angle $\gamma$ from the initial setting described above, the actual Bragg angle, $\theta_B$, for (001) planes is $\theta_B = \pi/2 - \gamma + (\alpha - \beta)$. The angle $(\alpha - \beta)$ was measured (away from the SRS) with the crystal mounted on a Bond-type orienting device (Bond, 1961), combining laser reflection from the nominal (001) facet with 004 reflections of Cu $K\alpha_1$ registered with a conventional X-ray goniometer; this measurement gave $(\alpha - \beta) = 0.95°$.

*Pendellösung* periods were measured on the following section topographs: (i) that shown on Fig. 8, (ii) one taken with the specimen setting illustrated in Figs. 10 and 11, and (iii) a repeat of (ii) after rotating the specimen 180° about its prism axis (parts of this section are shown in Fig. 12). In (i) only fringes in the right-hand wedge were deemed usable, due to the obscuration on the left attributed to surface strains, mentioned in §5. In (ii) the fringe patterns seen in both wedges resembled those in

**Table 1**

Absolute values of the diamond 004 structure factor derived from *Pendellösung* fringe spacing.

| Section topograph number | 1 | 2 | 2 | 3 | 3 |
|---|---|---|---|---|---|
| X-ray wavelength (nm) | 0.066 | 0.128 | 0.128 | 0.124 | 0.124 |
| X-ray entrance face | (b) | (a) | (b) | (d) | (c) |
| X-ray exit face | (c) | (d) | (c) | (a) | (b) |
| Orders of fringe maxima | 3–11 | 5–18 | 5–27 | 4–17 | 5–33 |
| $.1_m$ (µm) | 30.0 | 11.5 | 10.8 | 12.0 | 11.4 |
| $F(004)$ | 11.7 | 11.7 | 12.5 | 12.0 | 12.6 |

the corresponding wedge images in (iii) quite closely. Fringes in (i) were measured on ×25 enlargements on film using a precise glass scale read to 0.1 mm. In the case of (ii) and (iii) measurements were made on calibrated high-magnification (×249) positive prints using a specially



(a)



(b)
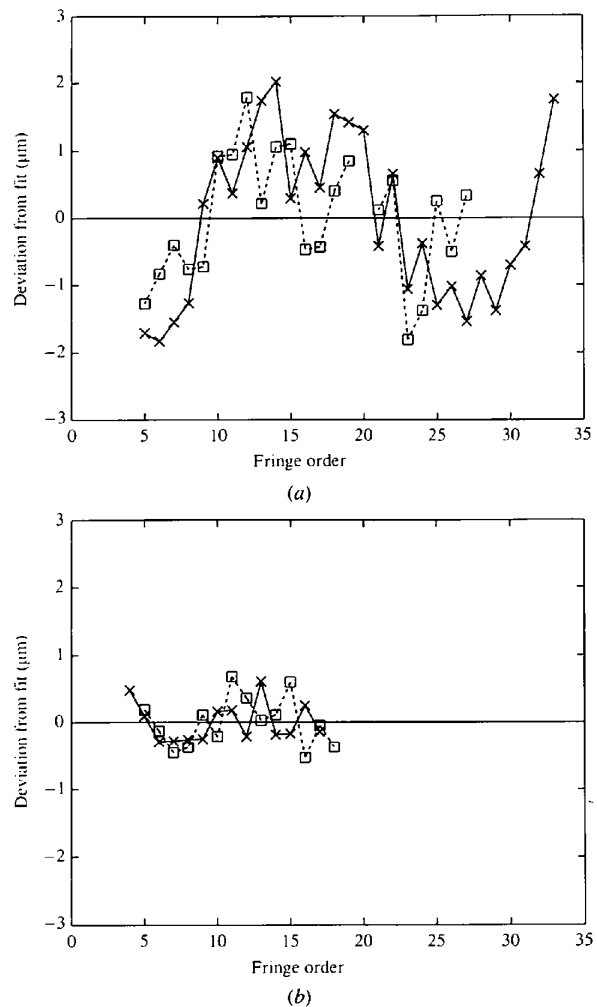
**Figure 13**
Expanded display of deviations of individual fringe positions from least-squares straight-line fits to plots of fringe position *versus* fringe order from which $F$ values were calculated. (a) Fringe systems in the wedge between faces (b) and (c): crosses show system summarized in Table 1, column 5; squares that in column 3 (absence of square at order 20 due to fringe obscuration by surface-damage-generated streak in plane of incidence). (b) Fringe systems in wedge between faces (a) and (d): crosses show system summarized in Table 1, column 4; squares that in column 2.

constructed glass cursor set against a steel scale, also read to 0.1 mm. The factor $\Phi$ was 0.493 in all cases, the angles $(c)^\wedge(b)$ and $(a)^\wedge(d)$ being closely similar. It is known that spacings of the first few fringes on section topographs are not constant (Homma, Ando & Kato, 1966), but these could not be measured in the present work because of specimen damage close to wedge edges. The ranges of fringe orders measured are listed in Table 1, where results of all measurements are set out. The fringe-order upper limit was determined by visibility loss and/or patent departure of $.1_m$ from constancy. On plots of positions of those fringes measured *versus* order, the linearity and regularity looked very satisfactory. More critically revealing, however, are plots (on an expanded scale) of deviations of individual measured fringe positions from the straight line fitted by least squares to each set of measurements. Such plots for topographs (ii) and (iii) are shown in Fig. 13. The impression of precision in structure-factor determination drawn from the good linearity within each set of measurements was confuted by the scatter in the five values of $F(004)$ resulting, roughly $\pm4\%$ about the mean value, $F(004) = 12.1$. This spread must be due to differences in the state of strain within the five volumes sampled, and cannot be attributed to imprecision in the measurement technique (believed to be good within $\pm1\%$). The topograph images present no compelling case for assigning different weights to the five measurements. Certainly there is higher irregularity of fringe positions in Fig. 13(a) compared with Fig. 13(b), but the former contains longer sequences for averaging. However, assuming that fringe perturbations by strain gradients will generally result in a reduction in mean $\Lambda_m$ (and hence higher calculated $F$), then the two high values 12.5 and 12.6, corresponding to the fringe sequences in Fig. 13(a), come under suspicion. Fringes produced by the harmonic 008 reflection would have a period three times greater than that of the observed fringes. No indication of a significant harmonic presence is detected.

Two other determinations of $F(004)$ with which this new determination can be compared are Göttlicher & Wölfel's (1959) powder-diffraction value, as slightly amended by Dawson (1967), $F(004) = 11.19$, and a recent finding on a single-crystal plate of synthetic diamond, $F(004) = 11.93$, by Takama, Tsuchiya, Kobayashi & Sato (1990) who observed *Pendellösung* oscillations with a source of unpolarized continuous radiation, and recorded, as a function of $\lambda$, the fringe orders at which the visibility fade due to superimposition of the $\sigma$- and $\pi$-fringe systems occurred (Hart & Lang, 1965; Hattori, Kuriyama & Kato, 1965).

## References

Bond, W. L. (1961). *J. Sci. Instrum.* **38**, 63–69.
Bowen, D. K. & Davies, S. T. (1983). *Nucl. Instrum. Methods*, **208**, 725–729.
Clark, C. D., Collins, A. T. & Woods, G. S. (1992). *The Properties of Natural and Synthetic Diamond*, edited by J. E. Field, pp. 35–79. London: Academic Press.
Davies, G. (1976). *J. Phys. C*, **9**, L537–542.
Dawson, B. (1967). *Proc. R. Soc. London Ser. A*, **278**, 264–287.
Göttlicher, S. & Wölfel, W. (1959). *Z. Elektrochem.* **63**, 891–901.
Hart, M. & Lang, A. R. (1965). *Acta Cryst.* **19**, 73–77.
Hattori, H., Kuriyama, H. & Kato, N. (1965). *J. Phys. Soc. Jpn*, **20**, 1047–1050.
Homma, S., Ando, Y. & Kato, N. (1966). *J. Phys. Soc. Jpn*, **21**, 1160–1165.
Kato, N. (1969). *Acta Cryst.* **A25**, 119–128.
Lang, A. R. (1993). *Diamond Relat. Mater.* **2**, 106–114.
Lang, A. R. (1994). *J. Appl. Cryst.* **27**, 988–1001.
Lang, A. R. (1995). *J. Phys. D*, **28**, A1–7.
Lang, A. R., Kowalski, G., Makepeace, A. P. W. & Moore, M. (1986). *Philos. Mag.* **B53**, L53–58.
Lang, A. R., Makepeace, A. P. W., Moore, M. & Machado, W. G. (1983). *J. Appl. Cryst.* **16**, 113–125.
Lang, A. R. & Pang, G. (1995). *J. Appl. Cryst.* **28**, 61–64.
Lang, A. R. & Pang, G. (1996). In preparation.
Lonsdale, K. (1947). *Philos. Trans. R. Soc. London Ser. A*, **240**, 219–250.
Takama, T., Tsuchiya, K., Kobayashi, K. & Sato, S. (1990). *Acta Cryst.* **A46**, 514–517.